

Effect of large-scale structures on wall shear stress fluctuations in pipe flow

Tong Tong, Kovid Bhatt, Tatsuya Tsuneyoshi, and Yoshiyuki Tsuji*

Department of Energy Engineering and Science, Nagoya University, Chikusa-ku, Furo-cho 464-8603, Japan

(Received 6 March 2020; accepted 31 August 2020; published 5 October 2020)

In this paper, particle image velocimetry and electrochemical measurements were applied simultaneously to examine the relationship between wall shear stress and the three-component velocity field in pipe flow. Moreover, the large-scale motions in the velocity field were separated into very-large-scale motions (VLSMs) and large-scale motions (LSMs) to investigate their respective influences on the wall shear stress fluctuations. The conditional velocity field during negative wall shear stress fluctuations confirmed the existence of the “footprints” of the streamwise and wall-normal velocity components in VLSMs. Further, a pair of counter-rotating roll modes was found to appear in the VLSMs, exhibiting length scales of $\lambda_x > 3R$, where λ_x is the streamwise wavelength and R is the pipe radius. In contrast, in LSMs, which exhibit length scales of $0.6R < \lambda_x < 3R$, counter-rotating vortex pairs were not observed. In this paper, the length-scale threshold for generating counter-rotating vortex pairs in pipe flow was found to be $3R$. This threshold value is higher than the value reported for turbulent boundary layers, which is 1δ , where δ is the boundary-layer thickness. Two-point correlations of wall shear stress, which are associated with the conditional spanwise velocity in the θ - x plane, revealed the effect of spanwise meandering features on the near-wall region.

DOI: [10.1103/PhysRevFluids.5.104601](https://doi.org/10.1103/PhysRevFluids.5.104601)**I. INTRODUCTION**

Mean wall shear stress has received extensive attention in both theoretical and experimental studies [1,2]. This subject is technologically important in engineering because of its association with energy dissipation by turbulence, through which energy is lost in moving flows along pipes, or when ships move through water or airplanes move through the air. According to recent statistical studies, wall shear stress fluctuations are considered important, as the ratio between the wall shear stress intensity and its mean, $\tau_{w,rms}^+ = \tau_{w,rms} / \overline{\tau_w}$, becomes almost constant at around 0.4 in a flow with a high Reynolds number [3,4].

During the last few decades, the scales of velocity structures in turbulence attracted considerable attention. The first study of large-scale structures in turbulence was carried out by Townsend [5], who found the existence of a long tail in the temporal correlation of the streamwise velocity in the flow of a turbulent boundary layer. In pipe flow, even though the flow motion is limited by the geometry of the pipe, the similarity of the long tail in the temporal correlation [6] indicates the existence of large-scale structures. Large-scale structures are defined as turbulent bulges in the boundary layer with an average length of $2-3\delta$ in the streamwise direction and $1-1.5\delta$ in the spanwise direction, where δ is the boundary-layer thickness [6]. Large-scale motions analogous to these bulges have been found in pipe flow and were as large as $2-4R$, where R is pipe radius [6]. Kim and Adrian [6] also reported that the statistically fluctuating streamwise velocity in pipe flow revealed long-wavelength peaks in the premultiplied energy spectra, which are termed “very-large-scale motions.” Similar results obtained by direct numerical simulation (DNS) confirmed the existence of long-

*Corresponding author: c42406a@cc.nagoya-u.ac.jp

wavelength structures [7], which are either large-scale motions (LSMs) or very-large-scale motions (VLSMs). In pipe flow, LSMs have been defined as motions exhibiting a streamwise wavelength up to $3R$, while VLSMs are those exhibiting longer wavelengths [8].

In the turbulent boundary layer, Hutchins and Marusic [9] observed that these VLSMs are elongated uniform-momentum regions that extend to large streamwise lengths and meander substantially in the spanwise direction. Furthermore, with the investigation of their three-dimensional structure, they found that the very-large-scale events maintain a “footprint” in the near-wall region. Therefore, it may be assumed that large-scale structures influence the near-wall physics of shear flows. Hutchins *et al.* [10] applied a spanwise array of hot-film probes together with a traversing hot wire and identified the relationship between large-scale skin-friction fluctuations with the streamwise length $\lambda_x > 0.5\delta$ (where λ_x is the wavelength in the streamwise direction) and velocity fluctuations in the turbulent boundary layer at a high Reynolds number. In their instantaneous shear stress data, the footprint of the large-scale structures in the near-wall region was comparable in scale to the superstructure events observed in the logarithmic (log) region of turbulent boundary layers.

It has been confirmed that these large-scale streamwise motions develop in the outer region (the log region of the velocity boundary layer) and become more prominent when the Reynolds number increases [6,11]. Furthermore, small-scale cycles in the near-wall region are influenced by the large-scale streamwise motion in the outer region by way of amplitude modulation effects [9]. Talluru *et al.* [12] extended the study of the amplitude modulation effects of large-scale motions into all three velocity components, based on the conditional averaged properties associated with negative large-scale skin-friction fluctuations ($\lambda_x > \delta$). They found that large-scale negative fluctuating streamwise structures are located between a pair of counter-rotating roll modes. Furthermore, they found that small-scale spanwise and vertical fluctuations, as well as the instantaneous Reynolds shear stress, are similarly modulated with the streamwise velocity fluctuations. Recently, Gomit *et al.* [13] performed a conditional sampling of the velocity at high Reynolds number based on a histogram of the wall shear stress fluctuations.

Following the confirmation of the influence of large-scale outer region structures on small cycles in the near-wall region, Mathis *et al.* [14] estimated the wall shear stress distribution by building a model that applied the low-frequency content of the streamwise velocity located in the log region. Spectra and second-order moments from their results demonstrated that the model successfully estimates the wall shear stress fluctuations. According to previous studies [9,10], it is known that, even though large-scale streamwise structures are generated in the log region and are more energetic there, their influence extends to the wall via a large-scale footprint in the near-wall region.

Studies are abundant for the average and statistical properties of wall shear stress in turbulence. However, the interaction between wall shear stress fluctuations and velocity fluctuations has not yet been thoroughly investigated. Using conditional averaging, the relationship between wall shear stress and the velocity field was qualitatively investigated by Talluru *et al.* [12] in the flow field of the turbulent boundary layer. However, in their study, the “large scale” ($\lambda_x > \delta$) contained both VLSMs and LSMs. The separate influences of VLSMs and LSMs on the wall shear stress have not yet been thoroughly studied.

In the present paper, simultaneous wall shear stress and particle image velocimetry (PIV) measurements were performed on pipe flows. The shear stress fluctuations were measured at eight locations along the circumference of the pipe, and the velocity fluctuations were obtained by PIV measurement at the pipe cross section. The shear stress fluctuations were measured using an electrochemical method that has been developed by several researchers [15]. We improved this technique and applied it to study turbulent structures in pipe flow [16,17]. Specifically, the contributions from the large-scale and very-large-scale motions to the wall shear stress fluctuations are discussed here. In contrast to the conditional averaging applied by Talluru *et al.* [12] and Gomit *et al.* [13], in the present paper, the velocity field was filtered to differentiate VLSMs and LSMs in order to distinguish their contributions to the wall shear stress fluctuations; then, a conditional averaging method was applied to examine the influences of VLSMs and LSMs on the negative wall shear stress fluctuations.

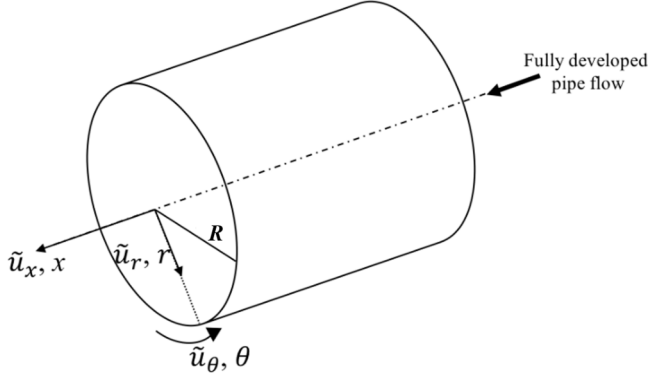


FIG. 1. Coordinate system of the pipe in the present paper.

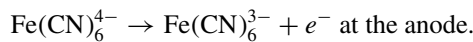
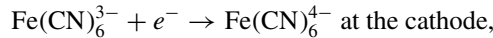
II. EXPERIMENTAL APPARATUS AND METHODS

The experimental loop and test section used in this paper were the same as the apparatus used by Tong *et al.* [16]. The coordinate system used in the present paper is shown in Fig. 1. In this figure, x is the flow direction, r is the radial direction, and θ is the azimuthal direction. The instantaneous velocity components in the streamwise, azimuthal, and radial directions are denoted \tilde{u}_x , \tilde{u}_θ , and \tilde{u}_r , respectively. And they are defined by their means and fluctuations as follows: $\tilde{u}_x = U_x + u_x$, $\tilde{u}_\theta = U_\theta + u_\theta$, and $\tilde{u}_r = U_r + u_r$. The superscript $+$ is used to refer to quantities normalized by the friction velocity u_τ and the viscosity ν . We specify the arc length and wall-normal distances as $s = r\theta$ and $y = R - r$, respectively, and refer to them as the spanwise and wall-normal directions, respectively.

A. The electrochemical method for wall shear stress measurement

In this paper, the wall shear stress was measured using an indirect method (the electrochemical technique), which measures the mass transfer rate and then uses this to calculate the wall shear stress, according to the method of Hanratty and Campbell [15]. The instantaneous wall shear stress is expressed by $\tilde{\tau}_w$, and the mass transfer rate is expressed by \tilde{k} . These instantaneous quantities are divided into their means and fluctuations such that $\tilde{\tau}_w = \bar{\tau}_w + \tau_w$ and $\tilde{k} = \bar{k} + k$.

In the electrochemical experiment, to measure the mass transfer rate, we used a three-electrode system [17], as shown in Fig. 2, which consisted of a cathode (as the working electrode), an anode (as the counter electrode), and a reference electrode. The test solution was an equilibrium mixture of potassium ferricyanide $[\text{K}_3\text{Fe}(\text{CN})_6]$ and potassium ferrocyanide $[\text{K}_4\text{Fe}(\text{CN})_6]$, with potassium sulfate (K_2SO_4) as the supporting electrolyte, the ions of which are not involved in the electrode reactions. The redox reactions of this system are as follows:



When a voltage is applied to an electrode, a redox reaction occurs on the electrode surface, and current flows through the circuit. The mass transfer rate \tilde{k} is obtained from the current by

$$\tilde{k} = i / A n_e F (c_b - c_w) \quad (1)$$

where c_b and c_w are the concentrations in the bulk and near the wall, respectively, A is the surface area of the electrode, n_e is the valence charge of an ion, F is the Faraday constant, and i is the current.

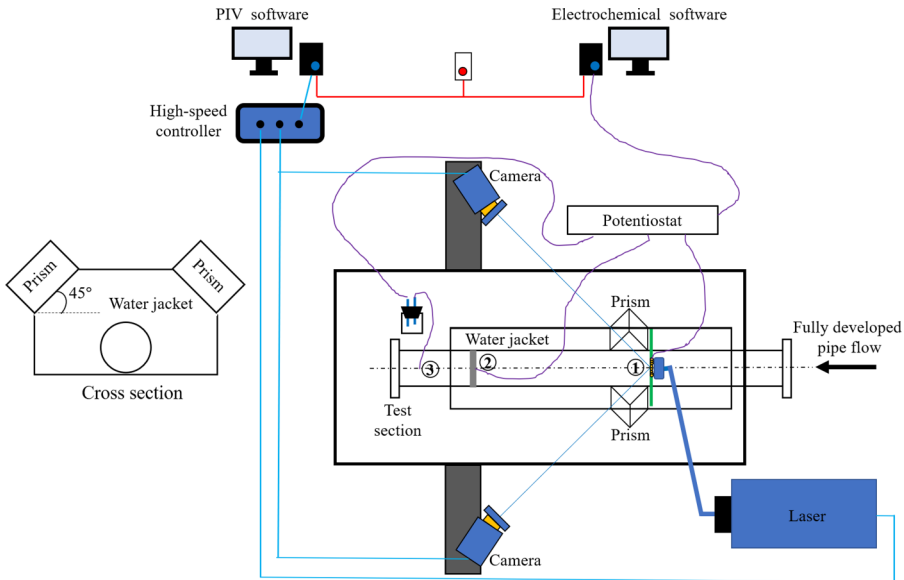


FIG. 2. Schematic view of the simultaneous measurement system. A stereo-PIV system was used to measure the three components of velocity at the cross section ①. Mass transfer fluctuations were measured by eight working electrodes mounted along the azimuthal direction at the same cross section as ①. The three-electrode system consisted of a cathode, an anode, and a reference electrode. These are indicated in the diagram as ① working electrode (cathode), ② counter electrode (anode), and ③ reference electrode.

Point circular electrodes were used for the measurement, as shown in Fig. 3. The electrodes were 1 mm in diameter, made of gold, and mounted on the pipe surface. They were insulated against the pipe wall at a distance of 0.3 mm. Acrylic resin was used as an insulating layer. For a point electrode, the concentration boundary layer develops only at its surface. Therefore, the length of the concentration boundary layer is equal to the length of the point electrode (details are provided in the previous report of Tong *et al.* [17]). In wall-bounded flow, the wall-shear stress detected by the electrode contains not only the streamwise component but also the spanwise and wall-normal components. All these three components of the signal are combined by the electrode.

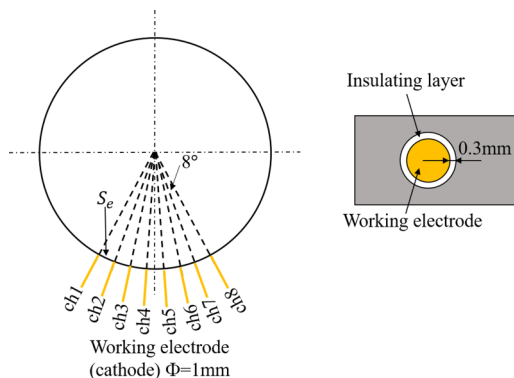


FIG. 3. Schematic view of the point electrode settings. The electrode diameter is 1 mm, and each electrode is separated by 8° . The electrode (yellow cylinder with a diameter of 1 mm) is mounted on the surface. The insulating layer is made of acrylic resin.

According to Hanratty and Campbell [15], if an electrode is small enough (a point electrode), the concentration boundary layer over the electrode surface will become so thin that it is located under the viscous sublayer of the velocity boundary layer. Under this condition, the velocity gradient \bar{S} can be estimated by the mass transfer rate \bar{k} as

$$\bar{k} = C \left(\frac{D_f^2 \bar{S}}{L} \right)^{1/3} \quad (2)$$

where L is the length of the electrode, D_f is the diffusion coefficient, and C is a constant. The wall shear stress $\bar{\tau}_w$ is calculated such that $\bar{\tau}_w = \mu \bar{S}$. Therefore, the relationship between the mass transfer rate and the wall shear stress can be given as

$$\bar{\tau}_w = \mu \bar{S} = C^{-3} \mu \frac{L \bar{k}^3}{D_f^2}. \quad (3)$$

In Eq. (3), the coefficient C includes the effect of the electrode shape and size. Hanratty and Campbell [15] gave one solution for the value of this coefficient: $C = 1.5/[9^{1/3} \Gamma(4/3)]$, where Γ is the gamma function; they used this solution to predict the mean wall shear stress according to several assumptions for a two-dimensional electrode. Even though Eq. (3) can be used to predict wall shear stress fluctuations based on the method of Hanratty and Campbell, this equation demonstrates large errors when used for flows with high frequency and large amplitude velocity fluctuations.

Previous studies detailed the measurement and principles of wall shear stress with the present experimental apparatus. Due to the finite area of the electrode, there is an attenuation of the signal over the electrode surface. In one study [17], to evaluate the effect of spatial resolution on the experimental measurement of wall shear stress fluctuations, a comparative study with DNS of channel flow [18] was conducted. From the comparison of the probability density functions and spectra of shear stress fluctuations with those of DNS data, it was found that the spatial and temporal resolutions in experiments were not identical to those in simulations. These differences were due to the finite size of the electrodes. However, it was also found that the wall shear stress fluctuations were measured accurately within the finite spatial and temporal resolutions of the electrode.

B. Simultaneous measurement

Figures 2 and 3 show a schematic view of the simultaneous measurement system. In the test section of straight pipe, eight working cathodes were inserted along the spanwise direction, and the angle between each electrode was 8° (equal to an arc length of $s_e = 0.14R$). The labels “ch1”–“ch8” are used to denote the positions of the working electrodes. All working cathodes were constructed from cylindrical gold wire with a diameter of 1 mm. The counter and reference electrodes were located far away from the working electrodes in the downstream region.

The stereo-PIV system consists of two digital high-speed complementary metal-oxide semiconductor cameras (High-Speed-Star 4G), an Nd:YLF laser, a high-speed controller, and a desktop personal computer to analyze the PIV data (the velocity fields were computed using the commercial PIV software DAVIS 8.1, which also operated the hardware of the PIV system). The inner diameter D and the wall thickness of the pipe were 46 and 2 mm, respectively. To ensure a fully developed flow, the upstream distance of the measurement area was approximately $90D$. The flow rate was measured by an electromagnetic flowmeter installed downstream of the test section. The optical distortion during the PIV measurements was reduced by securing a water jacket around the measurement area of the test section. In the stereo-PIV system, the camera needs to be installed obliquely to the target surface. However, under the constraints of the camera arrangement, the image reflected on the camera was distorted by the refractive index difference between the acrylic and the air. This distortion was reduced by installing a prism between the camera and the test section along the line of sight of the camera. The prism was made of 5-mm-thick acrylic, and its hollow interior was filled with water. Because the optical axis of each camera should be perpendicular to the prism surface, the prism was set at 45° to the horizontal line, as shown in Fig. 2. The flow was seeded

with fluorescent particles with a mean diameter of $15 \mu\text{m}$ and a density of 1.1 g/cm^3 . The flow was illuminated by a double-pulse Nd:YLF laser with an energy of 10 mJ/pulse and pulse duration was $450 \mu\text{s}$ for $\text{Re}_D = 25\,000$ and $250 \mu\text{s}$ for $\text{Re}_D = 45\,000$. The fluorescent particles were composed of rhodamine B, which is excited by wavelengths of approximately 550 nm when illuminated by a 527-nm laser and emits wavelengths longer than 580 nm .

The PIV images were recorded by two high-speed cameras with 1024×1024 pixel arrays ($17 \times 17 \mu\text{m}$ resolution) and a sampling rate of 1 kHz . The focal length of the camera lenses was 105 mm . The two cameras were configured following the angular-displacement method; that is, their axes were rotated inward so that they intersected at the midpoint of the measuring surface. In this configuration, because the object plane is not parallel to the lens plane, obtaining well-focused particle images across the image plane of the camera is rather difficult. To obtain well-focused images over the entire image plane, it was necessary to impose a Scheimpflug arrangement which requires collinearity of the object plane, the lens plane, and the image plane. Accordingly, a Scheimpflug adapter was added between each camera and its lens. To obtain bright and clear images of the flow field without reflection, each camera was equipped with a high-pass filter ($\lambda > 580 \text{ nm}$) in front of its lens; this filter admits only the fluorescent light scattered from the fluorescent particles. Measurements of the fluorescent particles are detailed in Yagi *et al.* [19].

In the data acquisition and calculations, the image pairs were analyzed using an iterative and adaptive multipass cross-correlation algorithm based on image reconstruction. To ensure that the correct particles were correlated and to minimize the number of erroneous vectors, we decreased the interrogation window size from 64×64 pixels in the initial passes to 32×32 pixels in the final passes.

As the flow field and wall shear stress were measured simultaneously, the PIV and electrochemical systems were set to the same sampling frequency. For both the PIV and electrochemical techniques, the measurement can be started by an external trigger signal. Therefore, a trigger switch was used to enable simultaneous measurement, as shown in Fig. 2. The experiment was performed at two Reynolds numbers $\text{Re}_D = 25\,000$ and $45\,000$ ($\text{Re}_D = U_m D/\nu$, where D is the pipe diameter and U_m is the cross-sectional mean streamwise velocity). The corresponding two friction Reynolds numbers were $\text{Re}_\tau = 696$ and 1140 , respectively, determined from the pipe radius R ($=D/2$) and the friction velocity u_τ ($\text{Re}_\tau = u_\tau R/\nu$). The sampling frequency was 1 kHz . To avoid overloading the memory of the high-speed cameras, we limited the number of images to 1360 per measurement. Thus, we obtained 5440 images from four measurement datasets and analyzed them along with the mass transfer rates collected at the eight electrodes. The ensemble average was calculated relative to each of the eight electrodes and the convergence was confirmed.

III. RESULTS AND DISCUSSION

A. Validation of sampling data

The data sets used in this paper include the sampling of wall shear stress and the three velocity components, as recorded by the simultaneous electrochemical and PIV measurements. Before the analysis, the data were validated against some fundamental properties.

For the wall shear stress measurement, the friction factor λ was used to determine the consistency of the mean wall shear stress measured in the present experiment. The λ values of the current experiment, those of the previous experiment [20], the DNS estimation [21], and the Blasius equation ($\lambda = 0.3164\text{Re}_D^{-0.25}$) are shown in Fig. 4. The similar friction factor values demonstrate the accuracy of the Blasius equation and the present wall shear stress measurements. Therefore, a calibration curve based on the Blasius equation was used to evaluate the wall shear stress fluctuations [17], as shown in Fig. 5. In this figure, the vertical axis shows the average mass transfer rate \bar{k} , measured by the electrochemical method, and the horizontal axis shows the mean wall shear stress $\bar{\tau}_w$, estimated from the Blasius equation. The green squares represent data from the present experimental results [Eq. (3)]. However, the parameter C in Eq. (3) is different from the value obtained by Hanratty and

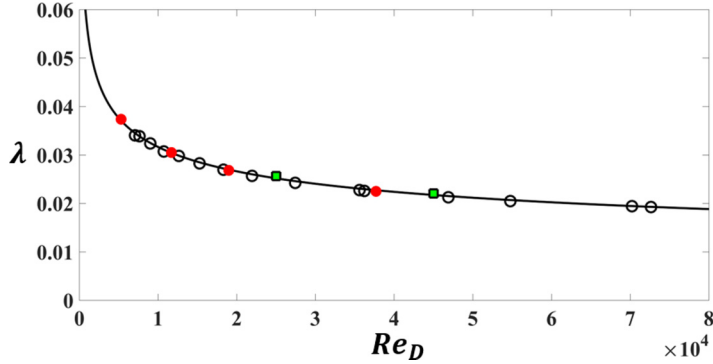


FIG. 4. Friction factor λ as a function of Re_D . The solid black line was derived using the Blasius equation. The solid red circles show the DNS results of Khoury *et al.* [21], the open circles show the experimental results of Furuichi *et al.* [20], and the green squares show the present experimental results.

Campbell [15]. In the present paper, the value of C was corrected according to the shape and size of the electrodes.

The spatial and time resolutions of the present shear stress measurement technique are discussed in Tong *et al.* [17]. A comparison of the DNS data indicates that the small-scale measurements are limited by the size of the electrode, which attenuates the spatial resolution, and by the shape of the electrode where a nonuniform concentration (or non-two-dimensional) boundary layer developed on the circular electrode surface. The spatial resolution becomes worse as the electrode size increases. The present electrode size is $d = 1$ mm, and the normalized space resolution is $d^+ \approx 30$ for $Re_\tau = 696$. The time resolution is not sufficient to resolve the small-scale fluctuations; however, the low-frequency fluctuations caused by the large-scale turbulent structures are well resolved.

In the PIV measurements, the spatial resolution was not high enough to resolve small-scale fluctuations, especially close to the wall. For the velocity field, the mean velocity profile of the streamwise velocity component U_x^+ ($U_x^+ = U_x/u_\tau$) was plotted against the distance from the wall y^+ ($y^+ = yu_\tau/\nu$) and compared with the DNS data [8,22], as shown in Fig. 6. The friction velocity was obtained by the calibration shown in Fig. 5. It is clear that the present PIV data match the DNS data in the log and wake regions from the second grid point against the wall. The second-order statistics of the turbulence intensities of the three velocity components are plotted in Fig. 7. The

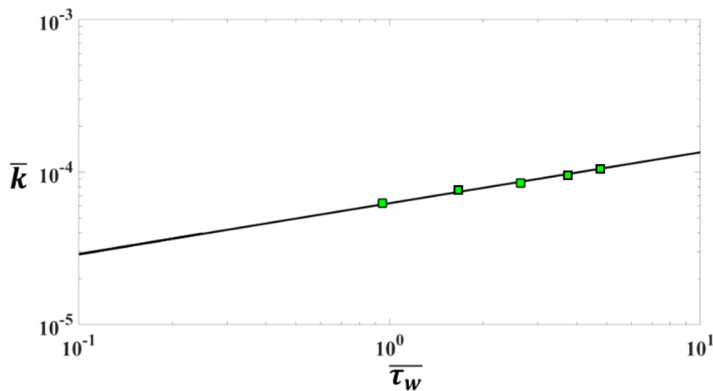


FIG. 5. Calibration curve for the wall shear stress measurement. The solid black line is the wall shear stress estimated by the Blasius equation, and the green squares indicate the present experimental results using Eq. (3) with a corrected value of C .

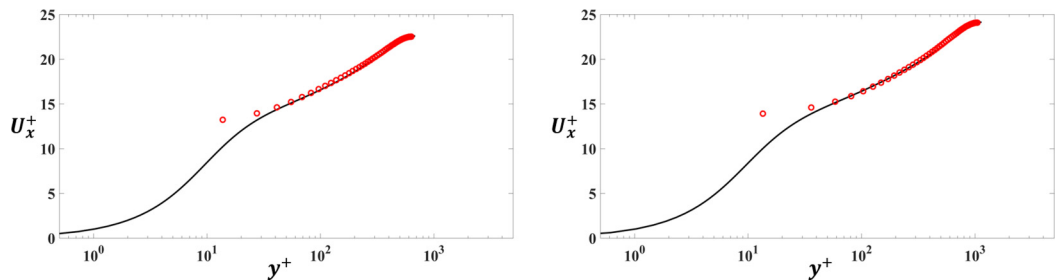


FIG. 6. Mean velocity profile of streamwise velocity U_x^+ as a function of y^+ ($= R^+ - r^+$). Black solid lines indicate the results of DNS (Wu *et al.* [8] for $Re_\tau = 685$; Wu and Moin [22] for $Re_\tau = 1142$). Red open circles indicate the present PIV measurements. (a) DNS, $Re_D = 24\,580$ ($Re_\tau = 685$); exp, $Re_D = 25\,000$ ($Re_\tau = 696$). (b) DNS, $Re_D = 44\,000$ ($Re_\tau = 1142$); exp, $Re_D = 45\,000$ ($Re_\tau = 1140$).

near-wall peaks in the present PIV measurements were very similar in magnitude and location to those found in previous DNS estimations [8,22]. The magnitude of $u_{x,rms}^+$ was slightly smaller in the present experiment when compared with the DNS results. The camera setting in our PIV system is shown in Fig. 2. It was oriented to accurately measure the cross-sectional velocity. A comparison with the DNS confirms that both u_r and u_θ components were obtained accurately (Fig. 7). However, the streamwise intensity was underestimated. This is due to the effect of the out-of-plane component on the streamwise velocity. The present PIV system adopts Cartesian coordinates (x, y, z) , which are converted into cylindrical coordinates (x, r, θ) for convenience. This process also increases the uncertainty in the data. Since we are interested in the cross-sectional motions, both u_r and u_θ components need to be measured accurately; this is confirmed in Fig. 7. As the streamwise component is used for the analysis based on Taylor's hypothesis, the streamwise mean velocity should be measured accurately. This is confirmed in Fig. 6. From these results, it is accepted that the present PIV system provides sufficient information to analyze the large-scale motions.

In the present paper, the influences of VLSMs and LSMs of the velocity field on near-wall-region events were investigated. Wu *et al.* [8] conducted direct numerical simulations of pipe flow and defined the length scale for distinguishing between VLSMs and LSMs based on the streamwise wavelength (VLSMs, $\lambda_x > 3R$; LSMs, $0.3R < \lambda_x < 3R$). According to this definition, in the present paper, the VLSMs ($\lambda_x > 3R$) of the velocity field were extracted using a low-pass filter, and the LSMs ($0.6R < \lambda_x < 3R$) were extracted based on the bandpass filter.

In the electrochemical experiments, the sampling data were contaminated by electrical noise. To establish the noise level, spectra of the wall shear stress were calculated, as shown in Fig. 8.

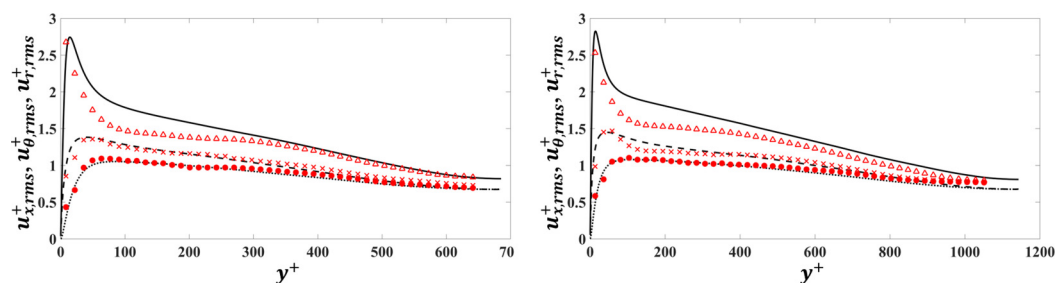


FIG. 7. Turbulence intensities against the wall. Black lines indicate the results of DNS (Wu *et al.* [8] for $Re_\tau = 685$; Wu and Moin [22] for $Re_\tau = 1142$), and red indicates the present PIV measurements. Solid lines and open triangles, $u_{x,rms}^+$; dashed lines and crosses, $u_{\theta,rms}^+$; dotted lines and solid circles, $u_{r,rms}^+$ as a function of y^+ ($= R^+ - r^+$). (a) DNS, $Re_D = 24\,580$ ($Re_\tau = 685$); exp, $Re_D = 25\,000$ ($Re_\tau = 696$). (b) DNS, $Re_D = 44\,000$ ($Re_\tau = 1142$); exp, $Re_D = 45\,000$ ($Re_\tau = 1140$).

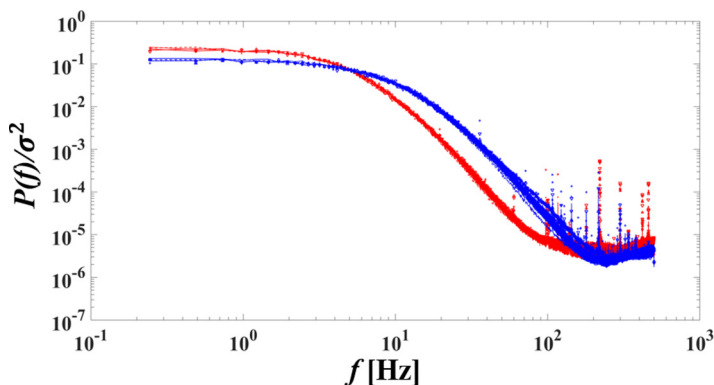


FIG. 8. Frequency spectra of the wall shear stress acquired by the eight electrodes (displayed as separate lines). Red, present measurements at $\text{Re}_D = 25\,000$ ($\text{Re}_\tau = 696$); blue, present measurements at $\text{Re}_D = 45\,000$ ($\text{Re}_\tau = 1140$).

The electrical noise was found to be present in the region with frequencies greater than 200 Hz. A low-pass filter was therefore applied to remove this noise.

B. Visualizations of velocity field and wall shear stress

Figure 9 shows the contours of wall shear stress and streamwise velocity fluctuations obtained from the simultaneous measurements. The time domain is converted to the spatial domain based on $x = U_m t$, where U_m is the cross-sectional mean streamwise velocity. The time series are changed into space fluctuations using Taylor's hypothesis. In general, the local mean velocity is adopted as the convection velocity; however, for the wall shear stress fluctuations, the appropriate convection velocity is not clear. Here, we adopt the cross-sectional velocity as the convection velocity to discuss the similar pattern generation in the wall shear stress and velocity fluctuations. In Sec. III C, the

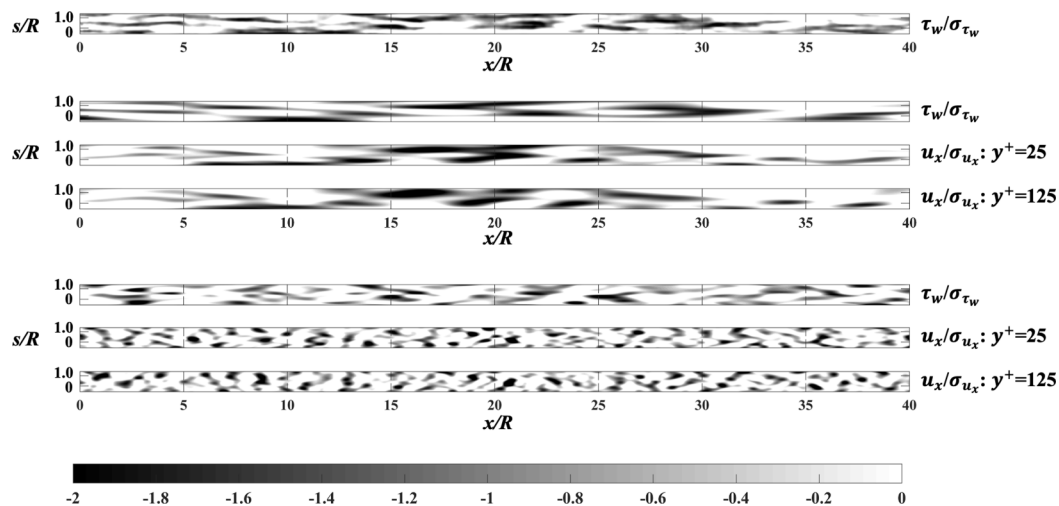


FIG. 9. Instantaneous negative fluctuations in wall shear stress and streamwise velocity at $\text{Re}_\tau = 1140$: (a) wall shear stress (raw), (b) VLSMs ($\lambda_x > 3R$) of wall shear stress and streamwise velocity, and (c) LSMs ($0.6R < \lambda_x < 3R$) of wall shear stress and streamwise velocity. Signals are projected along $x = U_m t$ and $s = r\theta$ as defined in Fig. 1.

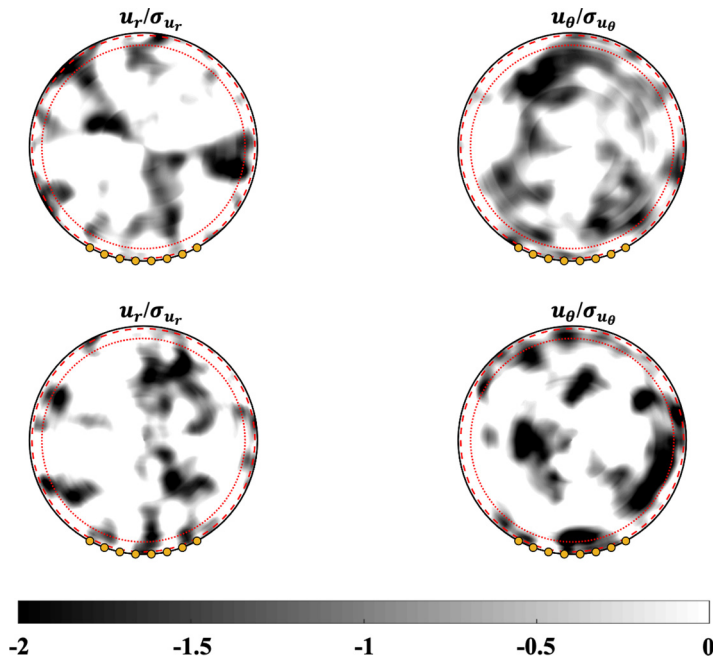


FIG. 10. Instantaneous negative fluctuations of u_r and u_θ at the position of $x/R = 20$, $\text{Re}_\tau = 1140$: (a) VLSMs ($\lambda_x > 3R$) and (b) LSMs ($0.6R < \lambda_x < 3R$). The red dashed lines show the position of $y^+ = 25$, and the red dotted lines show the position of $y^+ = 125$ (here, $y^+ = R^+ - r^+$). Solid yellow circles indicate the positions of the spanwise array of electrodes.

local mean velocity is adopted as the convection velocity to allow a quantitative discussion of the turbulent structures. The shadows in these plots are negative fluctuations (positive fluctuations are shown in white). Figure 9(a) shows the wall shear stress fluctuations measured from the spanwise array of electrodes. In this plot, it can be seen that the elongated regions clearly exhibit a length scale greater than $3R$. Figure 9(b) shows low-pass-filtered signals for $\lambda_x > 3R$, corresponding to the VLSMs. These are τ_w fluctuations and u_x fluctuations ($y^+ = 25$ and 125), in which both are very-large-scale structures of wall shear stress and velocity signals. The footprints of the VLSMs, which are generated in the log region, can be clearly seen, and these affect the wall shear stress fluctuations in the near-wall region. Figure 9(c) shows bandpass-filtered signals for $0.6R < \lambda_x < 3R$, corresponding to the LSMs of τ_w fluctuations and u_x fluctuations ($y^+ = 25$ and 125), in which both are large-scale structures of wall shear stress and velocity signals. In these instantaneous plots, distinguishing similar length-scale structures between the τ_w and u_x fluctuations is difficult. However, some high-magnitude areas in the u_x fluctuations exist, which are associated with the high-magnitude regions at similar positions to the τ_w fluctuations.

Figure 10 shows cross-sectional slices of u_r and u_θ at the corresponding position $x/R = 20$ of Fig. 9(a). In the figure, the shadow areas in the panels represent the negative fluctuations, whereas the positive fluctuations are indicated in white (see the axis directions of r and θ in Fig. 1). The contours of the VLSMs and LSMs of u_r and u_θ fluctuations in the wide area across the cross section indicate the effects of u_r and u_θ components on the τ_w fluctuations, especially above the electrode positions.

C. Conditional sampling

This paper used the conditional averaging method of Talluru *et al.* [12]. In their method, the skin-friction fluctuations were used as a “detector” probe for observing the events of the velocity

field. In Talluru *et al.*'s study, skin-friction fluctuations were filtered, but the velocity field was not. However, the present paper separately examines the effects of the VLSMs and LSMs on the wall shear stress fluctuations. To investigate how the VLSMs (or LSMs) of the velocity field affect the wall shear stress fluctuations, the velocity field was filtered to extract the VLSMs and LSMs and not the wall shear stress fluctuations. In high Re numbers, there is a scale separation between the inner small scales and the outer energetic large scales at the length scale δ . The outer scale is a concept concerning superstructures or attached eddies. Such large-scale motions play a significant role with respect to the wall shear stress [14]. If the effect of the superstructure is separately emphasized, low-pass filtering can be applied to the shear stress. However, the superstructures exist at high Re numbers, and their effects become small at moderate Re numbers, as reported in Mathis *et al.* [14]. Therefore, we did not apply a low-pass filter to the shear stress fluctuations.

The statistical convergence of conditional sampling is an important issue to be checked. We carefully did this before summarizing the results. The data were recorded by high-speed stereo PIV measurements at 1 kHz, and the total number of images is 5440 with 1360 images per run. This means that the total duration of the experiment is only 5.44 s. However, the ensemble average was done in relation with each of 8ch electrodes, and then the total data are $5.44 \times 8 = 43.5$ s. The cross-averaged velocity is approximately 0.6 m/s, and then the total length is $43.5 \times 0.6 = 26.1$ m, or $26.1 \text{ m}/R = 1180$. The total conditional sampling time for negative shear stress is approximately half of total conditional sampling time, that is, $43.5/2$ s. We confirmed the statistical convergence of conditional sampling.

1. Velocity field associated with VLSMs ($\lambda_x > 3R$)

To clarify the influence of VLSMs on the wall shear stress fluctuations, the relationship between τ_w (raw) and VLSMs of velocity in u_{xVL} , u_{rVL} , and $u_{\theta VL}$ components was investigated using the conditional properties of the velocity field based on negative wall shear stress events. As noted, VLSMs are recognized as motions with a length scale $\lambda_x > 3R$, based on the study of Wu *et al.* [8]. The instantaneous shear stress is divided into its mean and fluctuations such that $\tilde{\tau}_w = \overline{\tau}_w + \tau_w$, and negative wall shear stress events are defined as those in which the value of τ_w is negative and larger in magnitude than the mean value. From the simultaneous measurements of wall shear stress and the velocity field, the conditional velocity field is defined as

$$\begin{aligned} u_{xVL}|_n(\Delta x, \Delta \theta, r) &= \langle u_{xVL}(x, \theta, r) \mid \tau_w(x - \Delta x, \theta - \Delta \theta) < 0 \rangle, \\ u_{rVL}|_n(\Delta x, \Delta \theta, r) &= \langle u_{rVL}(x, \theta, r) \mid \tau_w(x - \Delta x, \theta - \Delta \theta) < 0 \rangle, \\ u_{\theta VL}|_n(\Delta x, \Delta \theta, r) &= \langle u_{\theta VL}(x, \theta, r) \mid \tau_w(x - \Delta x, \theta - \Delta \theta) < 0 \rangle \end{aligned} \quad (4)$$

where $u_{xVL}|_n$, $u_{rVL}|_n$, and $u_{\theta VL}|_n$ are the conditional very-large-scale velocity fluctuations based on the negative τ_w fluctuations. The time series are transformed to the spatial domain using Taylor's hypothesis $x = u_c t$, where u_c is the convection velocity, which is equal to the local mean velocity. Figures 11(a) and 11(b) show the contours of $u_{xVL}|_n$ and $u_{rVL}|_n$ in the r - x plane. Four cross-sectional slices were chosen at the locations $\Delta x/R = -1, 0, 1, \text{ and } 2$, as shown in Figs. 11(c) and 11(d).

Figure 11(a) shows the contours of the conditional VLSMs of the streamwise velocity component based on negative τ_w fluctuations, $u_{xVL}|_n$. A large-scale negative feature, extending to a length $> 3R$ in the streamwise direction, can clearly be seen. This result confirms the existence of very-large-scale streamwise velocity structures [10] in the pipe flow. In the upstream, a positive long-length region also appears, as shown in Fig. 11(a). This alternation of positive and negative regions of very-large-scale streamwise velocity structures may be attributed to the spanwise meandering of streamwise large-scale structures, as noted by Hutchins and Marusic [9]. The contours plotted in the cross section, as shown in Fig. 11(c), clearly exhibit the spanwise features of very-large-scale streamwise structures such that the negative fluctuation structure is flanked on each side by positive fluctuation structures. From Fig. 11(c), the width of the negative region is approximately $0.4R$ (approximately three times the arc length between two neighboring electrodes, $3s_e$), which is similar to the width of the corresponding negative region discovered in the flow of turbulent

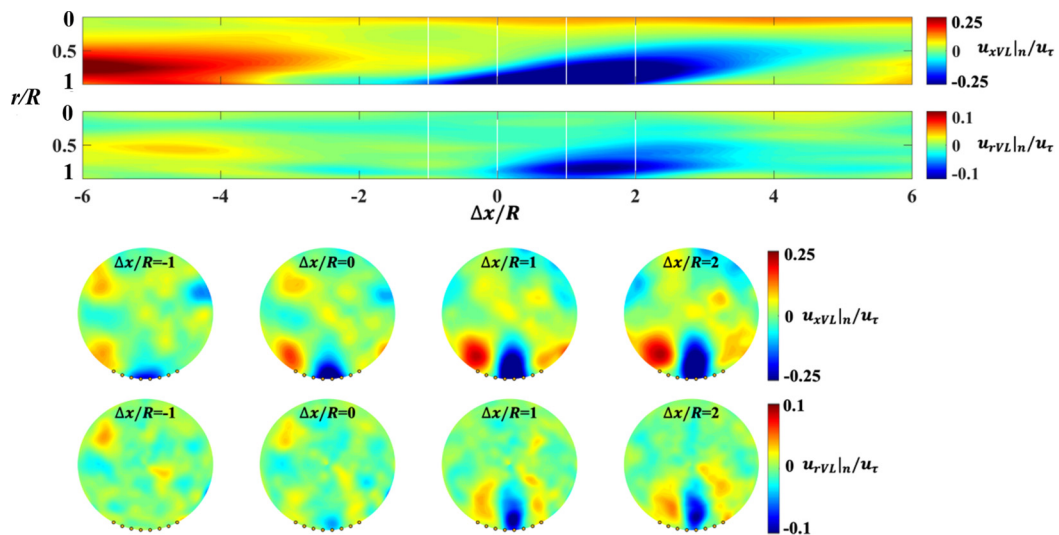


FIG. 11. Conditional velocity field of VLSMs ($\lambda_x > 3R$) during a negative wall shear stress event at $\text{Re}_\tau = 1140$: (a) contours of $u_{xV L}|_n$; (b) contours of $u_{rV L}|_n$ in the r - x plane, with streamwise distance calculated by the relation $x = u_c t$; (c) cross-sectional slices of $u_{xV L}|_n$ in the r - x plane at $\Delta x/R = -1, 0, 1$, and 2 ; and (d) cross-sectional slices of $u_{rV L}|_n$ in the r - x plane for $\Delta x/R = -1, 0, 1$, and 2 .

boundary layers [12]. To confirm the spanwise width of the very-large-scale streamwise structures, a two-point correlation of $u_{xV L}$ along the spanwise direction $R_{u_x u_x}$ at $y^+ = 25$,

$$R_{u_x u_x}(x, \Delta s) = \langle u_{xV L}(x, s) u_{xV L}(x, s - \Delta s) \rangle / \sigma_{u_x}^2, \quad (5)$$

was plotted and is shown in Fig. 12. According to a previous study [16], the threshold to define the spanwise typical length is 0.05. Using the same criteria here, the size of the positive correlation at $R_{u_x u_x} = 0.05$ is found as approximately $0.6R$. This length is slightly larger than the estimation of $u_{xV L}|_n$. This difference may be attributed to the spanwise feature of large-scale structures whereby the spanwise width increases with increasing the distance away from the wall [11].

Figure 11(b) shows the contours of conditional VLSMs of the wall-normal velocity component based on negative τ_w fluctuations, $u_{rV L}|_n$. A strong similarity exists between $u_{xV L}|_n$ and $u_{rV L}|_n$. This similarity reveals that in the motion of very-large-scale coherent structures, the negative $u_{xV L}$ -

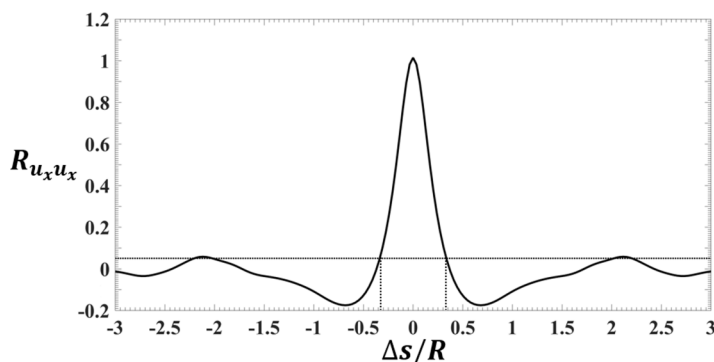


FIG. 12. Two-point correlation coefficient of $u_{xV L}$ along the spanwise direction at $y^+ = 25$ (here, $y^+ = R^+ - r^+$) and $\text{Re}_\tau = 1140$.

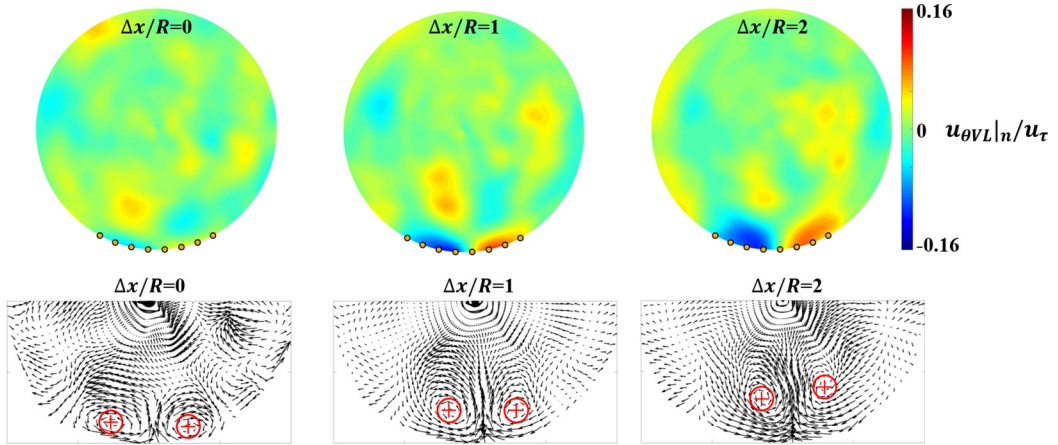


FIG. 13. (a) Cross-sectional slices of $u_{\theta VL}|_n$ at $\Delta x/R = 0, 1, \text{ and } 2$. (b) Counter-rotating roll modes acquired in the $u_{r VL}|_n$ and $u_{\theta VL}|_n$ vector fields in the cross-sectional slices at $\Delta x/R = 0, 1, \text{ and } 2$. The vortex core positions are marked by the symbol \oplus . $Re_{\tau} = 1140$.

fluctuation events are sprayed away from the wall. This is associated with negative $u_{r VL}$ -fluctuation events [flow away from the wall, see Fig. 11(d)]. From the cross-sectional slices of $u_{x VL}|_n$ and $u_{r VL}|_n$, it can be seen from Fig. 11(c) that the positive $u_{x VL}|_n$ events flanking the negative $u_{x VL}|_n$ events are also accompanied by positive $u_{r VL}|_n$ events (flow towards the wall). The motion of very-large-scale structures estimated based on the present results is consistent with the sketch of large-scale coherent flow motion in the boundary layer given by Marusic *et al.* [23]. From the contours of $u_{x VL}|_n$ and $u_{r VL}|_n$, it can be concluded that both $u_{x VL}$ and $u_{r VL}$ components exhibit a large-scale footprint in the near-wall region. However, the magnitude of $u_{r VL}|_n$ becomes smaller close to the wall, as shown in Fig. 11(b), which indicates the weaker energy of the $u_{r VL}$ component close to the wall.

The conditional velocity field of the VLSMs ($\lambda_x > 3R$) during a negative wall shear stress event, as plotted in Figs. 11(a) and 11(b), does not have a peak value at the reference point ($\Delta x = 0$). This is due to the time lag between the velocity and the wall shear stress. In the electrochemical method, the concentration boundary layer develops on the electrode surface and the velocity fluctuation affects the mass transfer rate through the concentration boundary layer. Therefore, the time lag between the velocity fluctuation and the wall shear stress fluctuation is attributed to the response of the concentration boundary layer. This point has been discussed in our previous study by Tong *et al.* [16] and Shan *et al.* [24].

Figure 13(a) shows the contours of $u_{\theta VL}|_n$ in a cross-sectional view for the corresponding locations in Fig. 11 at $\Delta x/R = 0, 1, \text{ and } 2$. Combining $u_{\theta VL}|_n$ and $u_{r VL}|_n$, the existence of large-scale counter-rotating roll modes can be seen, which were previously observed by Talluru *et al.* [12] in the flow of a boundary layer. The plotting of the $u_{r VL}|_n$ and $u_{\theta VL}|_n$ vector field clearly illustrates the counter-rotating pairs, as shown in Fig. 13(b). It can be concluded that, in a statistical sense, very-large-scale structures are located between a pair of counter-rotating vortices. In Fig. 13(b), the cores of the vortices are marked by the symbol \oplus . The cores of these vortices are away from the wall with the downstream location. This confirms the presence of very-large-scale structures inclined from the outer region to the near-wall region. Although the flow motions are limited by the geometry of the pipe, similar roll modes exist and are associated with very-large-scale velocity structures ($\lambda_x > 3R$). It is noted that in the boundary layer counter-rotating pairs appear, which are associated with the long velocity structures of $\lambda_x > \delta$ [12]. The comparable long-wavelength scale in pipe flow may be attributed to the constraints of the pipe geometry.

From the conditional velocity fields of VLSMs associated with negative wall shear stress fluctuations, it was found that the VLSMs demonstrate a strong character in the near-wall region,

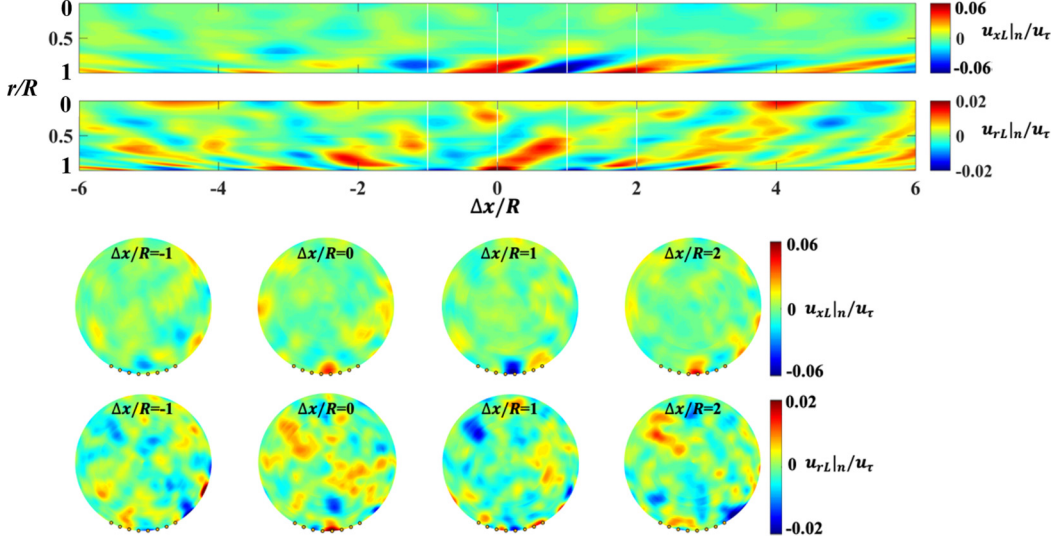


FIG. 14. Conditional velocity field of LSMs ($0.6R < \lambda_x < 3R$) during a negative wall shear stress event at $Re_\tau = 1140$: (a) contours of $u_{xL}|_n$ and (b) contours of $u_{rL}|_n$ in the r - x plane. Streamwise distance was calculated by the relation $x = u_\tau t$. (c) Cross-sectional slices of $u_{xL}|_n$ in the r - x plane at $\Delta x/R = -1, 0, 1,$ and 2 . (d) Cross-sectional slices of $u_{rL}|_n$ in the r - x plane at $\Delta x/R = -1, 0, 1,$ and 2 .

which was shown by a footprint in both the streamwise and wall-normal directions of velocity. This affects the wall shear stress fluctuations in the same direction of motion. From the cross-sectional view, a large-scale counter-rotating vortex pair of these footprints appears and exhibits an impact on the wall shear stress.

2. Velocity field associated with LSMs ($0.6R < \lambda_x < 3R$)

To clarify the influence of LSMs on the wall shear stress fluctuations, the relationship between τ_w (raw) and LSMs of velocity in the u_{xL} , u_{rL} , and $u_{\theta L}$ components was investigated using the conditional properties of the velocity field (for LSMs) based on a negative wall shear stress event. In the present paper, LSMs are defined as motions with a length scale $0.6R < \lambda_x < 3R$, based on the definition of Wu *et al.* [8]. Negative τ_w fluctuations are distinguished using only the sign of τ_w . From the simultaneous wall shear stress and velocity-field measurements, the conditional velocity field is defined as

$$\begin{aligned} u_{xL}|_n(\Delta x, \Delta \theta, r) &= \langle u_{xL}(x, \theta, r) \mid \tau_w(x - \Delta x, \theta - \Delta \theta) < 0 \rangle, \\ u_{rL}|_n(\Delta x, \Delta \theta, r) &= \langle u_{rL}(x, \theta, r) \mid \tau_w(x - \Delta x, \theta - \Delta \theta) < 0 \rangle, \\ u_{\theta L}|_n(\Delta x, \Delta \theta, r) &= \langle u_{\theta L}(x, \theta, r) \mid \tau_w(x - \Delta x, \theta - \Delta \theta) < 0 \rangle \end{aligned} \quad (6)$$

where $u_{xL}|_n$, $u_{rL}|_n$, and $u_{\theta L}|_n$ are the conditional large-scale velocities based on negative τ_w fluctuations. Figures 14(a) and 14(b) show cross-sectional views of the contours of $u_{xL}|_n$ and $u_{rL}|_n$ in the r - x plane. Four cross-sectional slices were chosen at the locations $\Delta x/R = -1, 0, 1,$ and 2 , as shown in Figs. 14(c) and 14(d).

Figure 14(a) shows the contours of conditional streamwise LSMs based on negative τ_w fluctuations. A large-scale negative feature with a length of approximately $1.5R$ can be seen in the streamwise direction. Positive long-length regions also appear, alternating with negative long-length regions, as shown in Fig. 14(a). This alternation of positive and negative large-scale fluctuation regions in the streamwise velocity structures also indicates the spanwise meandering feature of streamwise large-scale structures. The contours plotted in the cross section, as shown in Fig. 14(c), also exhibit the spanwise features of large-scale streamwise structures, in that the negative fluctua-

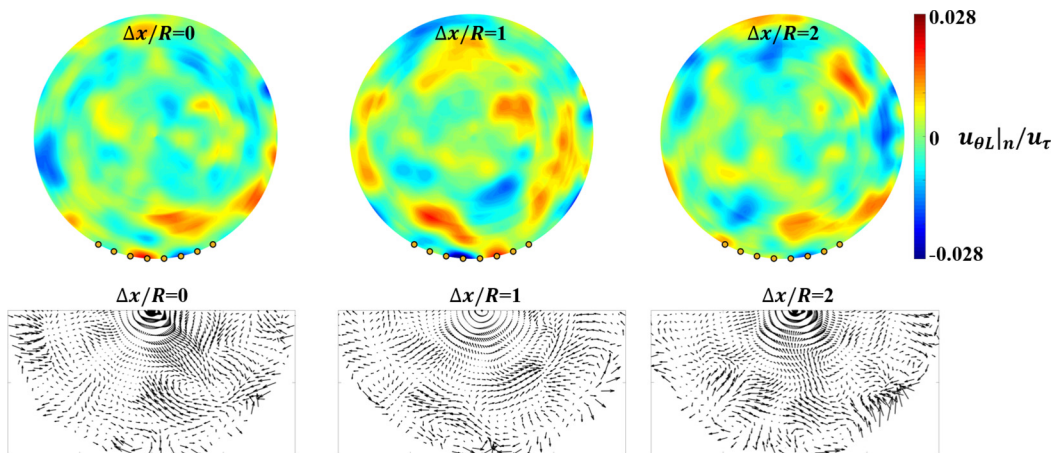


FIG. 15. (a) Cross-sectional slices of $u_{\theta L}|_n$ at $\Delta x/R = 0, 1, \text{ and } 2$. (b) Counter-rotating roll modes acquired in the $u_{rL}|_n$ and $u_{\theta L}|_n$ vector field in the cross-sectional slices at $\Delta x/R = 0, 1, \text{ and } 2$. $Re_{\tau} = 1140$.

tion structure is flanked on each side by positive fluctuation structures. From Fig. 14(c), the width of the negative region is approximately $0.2R$, which is half that of the VLSMs. By comparing the very-large-scale and large-scale structures, a difference can be seen not only in their streamwise lengths but also in their spanwise scales.

Figure 14(b) shows the contours of the conditional wall-normal direction of LSMs based on negative τ_w fluctuations. In contrast to the observations of $u_{xVL}|_n$ and $u_{rVL}|_n$, a strong similarity between $u_{xL}|_n$ and $u_{rL}|_n$ does not exist. This lack of similarity reveals that very weak energy of u_{rL} moves across the turbulence boundary layer to demonstrate an impact on the near-wall region. Therefore, in the near-wall cross section, as shown in Fig. 14(d), no obvious high-magnitude region exists in the contours of $u_{rL}|_n$. There is a time lag between the velocity and the wall shear stress fluctuations. Due to this time lag, the negative wall shear stress events are associated with the velocity field around $\Delta x/R \approx 1$. The negative velocity fluctuation relates to the negative wall shear stress fluctuation. This feature is confirmed in Fig. 11.

Figure 15(a) shows the contours of $u_{\theta L}|_n$ in the cross-sectional plane at the corresponding locations of Fig. 14 at $\Delta x/R = 0, 1, \text{ and } 2$. In further contrast to the VLSMs, combining $u_{\theta L}|_n$ and $u_{rL}|_n$, no pair of counter-rotating roll modes was found. From the plot of the vector field of $u_{rL}|_n$ and $u_{\theta L}|_n$, the lack of a counter-rotating vortex pair indicates that LSMs in pipe flow exhibit few features of vertical motion (flow away from or towards the wall).

From the conditional velocity field of LSMs associated with negative wall shear stress fluctuations, only the streamwise direction of LSMs exhibits a footprint in the near-wall region, affecting the wall shear stress. In the present paper, the wavelength required for the appearance of a pair of counter-rotating roll modes in pipe flow was found to be larger than $3R$.

The conditional sampling process is not the same as that of Talluru *et al.* [12]. We separate the velocity fluctuations into large-scale fluctuations u_L and very-large-scale fluctuations u_{VL} , and then these fluctuations are conditionally averaged with negative shear stress by Eqs. (4) and (6). From this conditional averaging, we understand the difference between the LSMs and VLSMs, and how they contribute to the negative shear stress. On the other hand, Talluru *et al.* [12] separate the shear stress fluctuation into large and small scales. The large-scale fluctuations, which are larger than boundary-layer thickness, are only adopted in their study, and the velocity signals are conditionally averaged by the negative large-scale shear stress fluctuations. From the conditional sampling of Talluru *et al.* [12], we can understand how the large-scale negative shear stress is linked with the velocity field. In these two studies, the velocity field is averaged by negative shear stress, but their objectives are different. It is also noted that the velocity field in the present paper is measured for

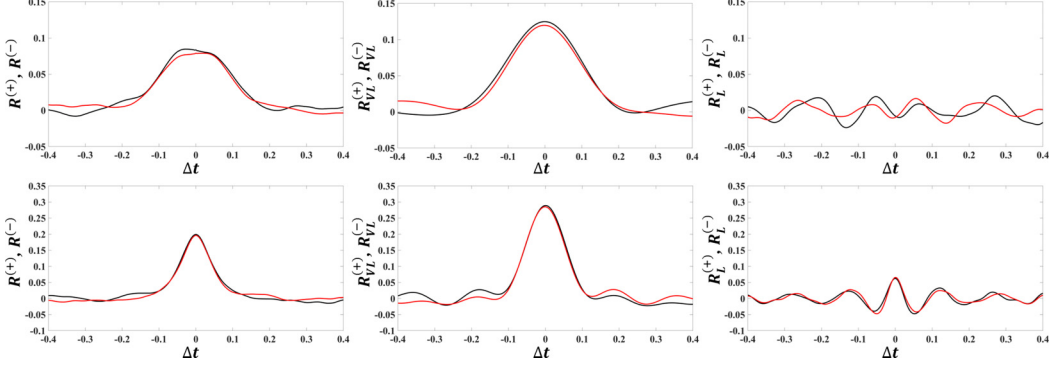


FIG. 16. Two-point correlations of wall shear stress. Red lines indicate the correlation coefficients of $R^{(+)}(\Delta t)$, $R_{VL}^{(+)}(\Delta t)$, and $R_L^{(+)}(\Delta t)$. Black lines indicate the correlation coefficients of $R^{(-)}(\Delta t)$, $R_{VL}^{(-)}(\Delta t)$, and $R_L^{(-)}(\Delta t)$. The left panels show the raw wall shear stress fluctuations τ_w , the central panels show very-large-scale fluctuations ($\lambda_x > 3R$) τ_{wVL} , and the right panels show large-scale fluctuations ($0.6R < \lambda_x < 3R$) τ_{wL} . (a) $\text{Re}_\tau = 696$. (b) $\text{Re}_\tau = 1140$.

pipe flow at moderate Re number, and in the study by Talluru *et al.* [12] it is measured for the turbulent boundary layer at high Re number.

3. Spanwise meandering

To detect the spanwise motion of coherent structures in the near-wall region, a two-point correlation of wall shear stress between two neighboring electrodes of the spanwise array was defined as follows. These equations represent the correlations of the original wall shear stress, the wall shear stress conditioned by VLSMs, and the wall shear stress conditioned by LSMs:

$$R^{(+)}(\Delta t) = \frac{1}{6} \sum_{n=2}^7 \frac{\langle \tau_{w,n}(t) \tau_{w,n+1}(t + \Delta t) \rangle}{\sigma_n \sigma_{n+1}},$$

$$R^{(-)}(\Delta t) = \frac{1}{6} \sum_{n=2}^7 \frac{\langle \tau_{w,n}(t) \tau_{w,n-1}(t + \Delta t) \rangle}{\sigma_n \sigma_{n-1}}, \quad (7)$$

$$R_{VL}^{(+)}(\Delta t) = \frac{1}{6} \sum_{n=2}^7 \frac{\langle \tau_{wVL,n}(t) \tau_{wVL,n+1}(t + \Delta t) \rangle}{\sigma_n \sigma_{n+1}},$$

$$R_{VL}^{(-)}(\Delta t) = \frac{1}{6} \sum_{n=2}^7 \frac{\langle \tau_{wVL,n}(t) \tau_{wVL,n-1}(t + \Delta t) \rangle}{\sigma_n \sigma_{n-1}}, \quad (8)$$

$$R_L^{(+)}(\Delta t) = \frac{1}{6} \sum_{n=2}^7 \frac{\langle \tau_{wL,n}(t) \tau_{wL,n+1}(t + \Delta t) \rangle}{\sigma_n \sigma_{n+1}},$$

$$R_L^{(-)}(\Delta t) = \frac{1}{6} \sum_{n=2}^7 \frac{\langle \tau_{wL,n}(t) \tau_{wL,n-1}(t + \Delta t) \rangle}{\sigma_n \sigma_{n-1}} \quad (9)$$

where τ_w is the raw wall shear stress fluctuations, τ_{wVL} is the wall shear stress filtered for very-large-scale structures ($\lambda_x > 3R$), and τ_{wL} is the wall shear stress filtered for large-scale structures ($0.6R < \lambda_x < 3R$). The subscript n indicates the channel number of the electrode, and the shear stress was recorded for 30 min.

Hutchins and Marusic [9] found that instantaneous large-scale streamwise fluctuations in the log region meander substantially along its length. Statistically, we can picture that if these meandering

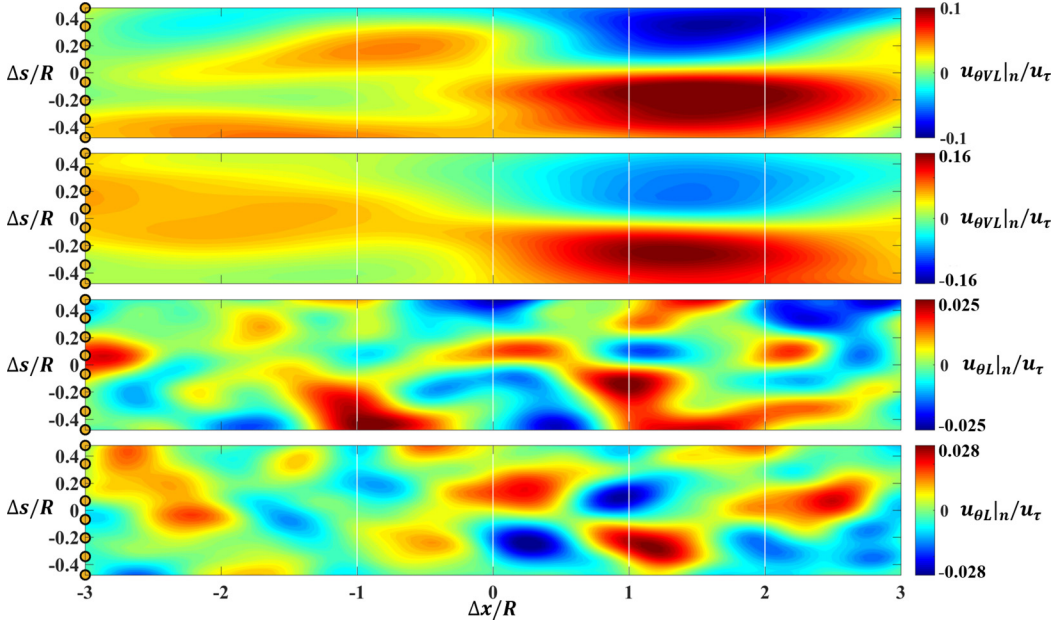


FIG. 17. Conditional velocity field of spanwise components during a negative wall shear stress event in the θ - x plane: (a) the contours of VLSMs $u_{\theta VL}|_n$ at $y^+ = 15$ for $Re_\tau = 696$; (b) the contours of VLSMs $u_{\theta VL}|_n$ at $y^+ = 25$ for $Re_\tau = 1140$; (c) the contours of LSMs $u_{\theta L}|_n$ at $y^+ = 15$ for $Re_\tau = 696$; and (d) the contours of LSMs $u_{\theta L}|_n$ at $y^+ = 25$ for $Re_\tau = 1140$. Signals were projected along $x = u_c t$.

features are symmetric in the spanwise direction, when they affect the wall shear stress in the near-wall region, the peak of the two-point correlation coefficient of the wall shear stress spanwise array should be located at $\Delta t = 0$. Figure 16(a) shows two-point correlations of wall shear stress at $Re_\tau = 696$. The panels from left to right show the two-point correlations of τ_w , τ_{wVL} , and τ_{wL} , respectively. It can be seen that for a low Reynolds number the correlation coefficients $R_{VL}^{(+)}(\Delta t)$ and $R_{VL}^{(-)}(\Delta t)$ of very-large-scale fluctuations τ_{wVL} overlap with each other, and their peak value is located at $\Delta t = 0$. This indicates that the symmetric meandering features of very-large-scale structures exist in the near-wall region, affecting the wall shear stress. However, in the large-scale fluctuations τ_{wL} , the correlation coefficients $R_L^{(+)}(\Delta t)$ and $R_L^{(-)}(\Delta t)$ do not overlap, and peak values do not typically appear. This small two-point correlation of τ_{wL} indicates that for a low Reynolds number large-scale coherent structures of the near-wall region perform an irregular meandering motion in the spanwise direction. These irregular spanwise motions exhibit a strong effect on the wall shear stress fluctuations, since the correlation coefficients $R^{(+)}(\Delta t)$ and $R^{(-)}(\Delta t)$ of the raw wall shear stress τ_w exhibit nonobvious peak values.

Figure 16(b) shows two-point correlations of wall shear stress at $Re_\tau = 1140$. The panels from left to right show the two-point correlations of τ_w , τ_{wVL} , and τ_{wL} , respectively. It can be seen that in both very-large-scale fluctuations τ_{wVL} and large-scale fluctuations τ_{wL} typical peak values exist, which are located at $\Delta t = 0$. Moreover, the correlation coefficients of $R^{(+)}(\Delta t)$ and $R^{(-)}(\Delta t)$ overlap with each other. This indicates that with a high Reynolds number symmetric spanwise meandering features exist in both the very-large-scale and large-scale structures in the near-wall region.

To confirm the estimations of the spanwise meandering features in the near-wall region in the flow field with low and high Reynolds numbers, the contours of the conditional averaged spanwise velocity components $u_{\theta VL}|_n$ and $u_{\theta L}|_n$ were plotted in the θ - x plane in the near-wall region. Figures 17(a) and 17(b) show the VLSMs of $u_{\theta VL}|_n$ for $Re_\tau = 696$ and $Re_\tau = 1140$, respectively.

These plots are consistent with the conclusions from the two-point correlations and show that the VLSMs exhibit symmetric spanwise meandering features. Figure 17(c) shows the LSMs of $u_{\theta L}|_n$ for $Re_\tau = 696$. It was found that spanwise meandering features of LSMs were irregular in the flow field with a low Reynolds number. This is consistent with the findings of the two-point correlation of τ_{wL} at $Re_\tau = 696$. However, the LSMs visible in the flow field with a high Reynolds number exhibit a very clear symmetry of positive and negative regions of $u_{\theta L}|_n$, as shown in Fig. 17(d). This indicates that with a high Reynolds number symmetric spanwise meandering features exist in large-scale structures in the near-wall region.

The two-point correlations of wall shear stress fluctuations (very-large-scale and large-scale), associated with the conditional velocity fields of $u_{\theta VL}|_n$ and $u_{\theta L}|_n$ in the θ - x plane, revealed that the symmetric spanwise meandering features of VLSMs affect the near-wall region, in turn affecting the wall shear stress fluctuations. However, even though the LSMs of the flow field with a high Reynolds number exhibit clear symmetric spanwise meandering features in the near-wall region, with a low Reynolds number, spanwise meandering features become irregular.

IV. CONCLUSIONS

Simultaneous electrochemical and PIV measurements were used to investigate the influence of VLSMs ($\lambda_x > 3R$) and LSMs ($0.6R < \lambda_x < 3R$) on wall shear stress fluctuations. Moreover, not only the streamwise velocity component but also the wall-normal and spanwise directions were investigated to find their relationships with wall shear stress fluctuations.

The instantaneous contours of wall shear stress fluctuations and very-large-scale ($\lambda_x > 3R$) streamwise velocity fluctuations exhibited strong similarity in negative fluctuation structures. This is consistent with the results of previous studies [10,16]. Furthermore, the wall-normal and spanwise velocity components showed areas of strong fluctuation that were associated with strong fluctuations in the wall shear stress. This indicates that u_r and u_θ components also exhibit influence on the fluctuations in τ_w . However, large-scale ($0.6R < \lambda_x < 3R$) streamwise velocity fluctuations did not exhibit strong evidence for any similarity with the wall shear stress fluctuation in the instantaneous view.

From the conditional velocity fields associated with negative wall shear stress fluctuations, it can be concluded that, in a statistical sense, very-large-scale velocity events exhibit a three-dimensional nature. The footprints of $u_{xVL}|_n$ and $u_{rVL}|_n$ confirmed the effect of large-scale structures, generated in the log region, on the near-wall events. The existence of a pair of counter-rotating vortices observed in the vector fields of $u_{rVL}|_n$ and $u_{\theta VL}|_n$ confirmed the model of Marusic *et al.* [23], which showed that large-scale structures are located between a pair of counter-rotating large-scale roll modes. However, in the conditional LSMs, a counter-rotating vortex pair was not observed in the vector fields of $u_{rL}|_n$ and $u_{\theta L}|_n$, which indicates that only the streamwise velocity of LSMs exhibits a footprint in the near-wall region, affecting the wall shear stress. In the present paper, the wavelength threshold for the appearance of counter-rotating vortex pairs in the pipe flow was $3R$, which was larger than the wavelength of 1δ found in the flow of turbulent boundary layers reported by Marusic *et al.* [23].

The spanwise motions of coherent structures in the near-wall region associated with the conditional spanwise velocity components of $u_{\theta VL}|_n$ and $u_{\theta L}|_n$ in the θ - x plane were estimated using two-point correlations of wall shear stress from the spanwise array. From these results, VLSMs in flow fields with both a low and a high Reynolds number were found to exhibit symmetric spanwise meandering features. However, LSMs in a flow field with a low Reynolds number did not exhibit symmetric spanwise meandering features. This was in contrast to LSMs in a flow field with a high Reynolds number, which showed clear spanwise symmetry of positive and negative regions in $u_{\theta L}|_n$ in the downstream direction.

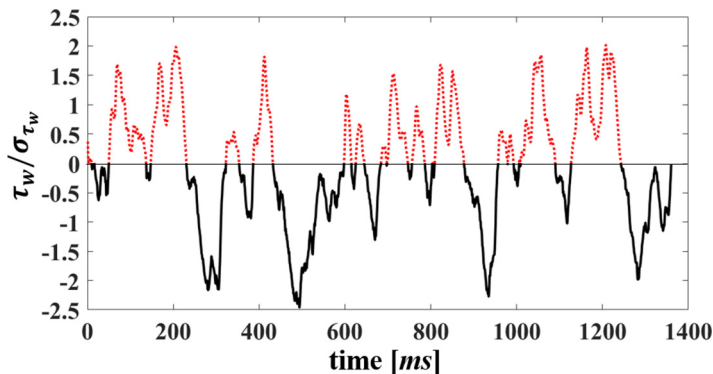


FIG. 18. Example of wall shear stress fluctuations at $Re_D = 45\,000$ ($Re_\tau = 1140$). Signals are low-pass filtered with 200 Hz. The solid line and dashed line indicate the negative and positive fluctuation parts, respectively.

ACKNOWLEDGMENTS

We appreciate the experimental support from Prof. F. Shan (Huazhong University of Science and Technology), T. Hayashi and L. Z. Chen through the research. This work is partially supported by the “Nagoya University High Performance Computing Research Project for Joint Computational Science” in Japan. Financial support from Leadership Development Program for Space Exploration and Research, and JSPS KAKENHI Grant No. 19H00747 are gratefully acknowledged.

APPENDIX: FREQUENCY RESPONSE OF SHEAR STRESS MEASUREMENT

In our measurement, the shear stress fluctuations (especially the high-frequency parts) are space averaged over the electrode surface. The surface area is not small, therefore the space averaged signals become smooth and high-frequency fluctuations are not contained. The example of shear stress fluctuation is plotted in Fig. 18. With the low-pass filter at 200 Hz, it does not show any frequent changes (or spikelike signal) around zero. From this signal, it is observed that negative fluctuations consist of large-scale motions, but positive ones show smaller-scale motions.

In the electrochemical measurement, the evaluation of the time-frequency response is an important issue that has been investigated by many researchers so far [25]. Different from the hot-wire technique, we cannot easily perform the impulse-response diagnostics. The previous studies show that the frequency response is evaluated by the normalized frequency f^+ as

$$f^+ = \frac{\ell^2}{D_f(S^+)^{2/3}} f \quad (\text{A1})$$

where ℓ is the electrode size, D_f is a diffusion coefficient [26], and S is a shear stress fluctuation normalized as $S^+ = (S\ell^2)/D_f$. The progressive damping occurs around $f^+ = O(1)$ until high frequencies, and phase delay also appears. It is clear how the electrode length can be smaller with the mass transfer probes, which improves the frequency response. This frequency response is evaluated in a laminar state using the rectangular electrode. The concentration boundary layer is two dimensional and develops in the downstream on the electrode. However, in turbulent flow, the situation becomes complex. The concentration boundary layer does not develop in two dimensions instantaneously, shear stress fluctuation becomes large, and the electrode shape significantly affects the mass transfer rate. Because of these factors, there are discrepancies between different theoretical predictions and different experimental results for the frequency response. A consensus has not been obtained so far [27,28].

Based on Eq. (A1) and the previous study [17] in comparison with DNS data, we estimate the time-frequency response in the present paper, and it is several tens of hertz. The signal higher than 100 Hz attenuates suddenly until 1-kHz sampling frequency.

-
- [1] H. Fernholz and P. Finley, The incompressible zero-pressure-gradient turbulent boundary layer: An assessment of the data, *Prog. Aerosp. Sci.* **32**, 245 (1996).
 - [2] P. A. Monkewitz, K. A. Chauhan, and H. M. Nagib, Self-consistent high-Reynolds-number asymptotics for zero-pressure-gradient turbulent boundary layers, *Phys. Fluids* **19**, 115101 (2007).
 - [3] P. H. Alfredsson, A. V. Johansson, J. H. Haritonidis, and H. Eckelmann, The fluctuating wall-shear stress and the velocity field in the viscous sublayer, *Phys. Fluids* **31**, 1026 (1988).
 - [4] R. Örlü and P. Schlatter, On the fluctuating wall-shear stress in zero pressure-gradient turbulent boundary layer flows, *Phys. Fluids* **23**, 021704 (2011).
 - [5] A. A. Townsend, The turbulent boundary layer, in *Grenzschichtforschung/Boundary Layer Research*, edited by H. Görtler (Springer-Verlag, Berlin, Heidelberg, 1958), pp. 1–15.
 - [6] K. C. Kim and R. J. Adrian, Very large-scale motion in the outer layer, *Phys. Fluids* **11**, 417 (1999).
 - [7] M. Guala, S. E. Hommema, and R. J. Adrian, Large-scale and very-large-scale motions in turbulent pipe flow, *J. Fluid Mech.* **554**, 521 (2006).
 - [8] X. Wu, J. R. Baltzer, and R. J. Adrian, Direct numerical simulation of a 30R long turbulent pipe flow at $R^+ = 685$: Large-and very large-scale motions, *J. Fluid Mech.* **698**, 235 (2012).
 - [9] N. Hutchins and I. Marusic, Evidence of very long meandering features in the logarithmic region of turbulent boundary layers, *J. Fluid Mech.* **579**, 1 (2007).
 - [10] N. Hutchins, J. P. Monty, B. Ganapathisubramani, H. C. H. Ng, and I. Marusic, Three-dimensional conditional structure of a high-Reynolds-number turbulent boundary layer, *J. Fluid Mech.* **673**, 255 (2011).
 - [11] J. P. Monty, J. A. Stewart, R. C. Williams, and M. S. Chong, Large-scale features in turbulent pipe and channel flows, *J. Fluid Mech.* **589**, 147 (2007).
 - [12] K. M. Talluru, R. Baidya, N. Hutchins, and I. Marusic, Amplitude modulation of all three velocity components in turbulent boundary layers, *J. Fluid Mech.* **746**, R1 (2014).
 - [13] G. Gomit, R. de Kat, and B. Ganapathisubramani, Structure of high and low shear-stress events in a turbulent boundary layer, *Phys. Rev. Fluids* **3**, 014609 (2018).
 - [14] R. Mathis, I. Marusic, S. I. Chernyshenko, and N. Hutchins, Estimating wall-shear-stress fluctuations given an outer region input, *J. Fluid Mech.* **715**, 163 (2013).
 - [15] T. J. Hanratty and J. A. Campbell, Measurement of wall shear stress, in *Fluid Mechanics Measurements*, 2nd ed., edited by R. J. Goldstein (Taylor & Francis, Philadelphia, PA, 1996), pp. 575–648.
 - [16] T. Tong, T. Tsuneyoshi, T. Ito, and Y. Tsuji, Instantaneous mass transfer measurement and its relation to large-scale structures in pipe flow, *Int. J. Heat Fluid Flow* **71**, 160 (2018).
 - [17] T. Tong, T. Tsuneyoshi, and Y. Tsuji, Shear stress fluctuation measurements using an electrochemical method in pipe flow, *J. Fluid Sci. Technol.* **14**, JFST0013 (2019).
 - [18] A. Mehrez, J. Philip, Y. Yamamoto, and Y. Tsuji, Pressure and spanwise velocity fluctuations in turbulent channel flows: Logarithmic behavior of moments and coherent structures, *Phys. Rev. Fluids* **4**, 044601 (2019).
 - [19] T. Yagi, A. Kamoda, A. Sato, W. Yang, and M. Umezu, 3D volume flow visualization for vascular flow modelling using stereo PIV with fluorescent tracer particles, paper presented at the 8th International Symposium on Particle Image Velocimetry (PIV 09), Melbourne, Australia, 2009 (unpublished).
 - [20] N. Furuichi, Y. Terao, Y. Wada, and Y. Tsuji, Friction factor and mean velocity profile for pipe flow at high Reynolds numbers, *Phys. Fluids* **27**, 095108 (2015).

- [21] G. K. El Khoury, P. Schlatter, A. Noorani, P. F. Fischer, G. Brethouwer, and A. V. Johansson, Direct numerical simulation of turbulent pipe flow at moderately high Reynolds numbers, *Flow, Turbul. Combust.* **91**, 475 (2013).
- [22] X. Wu and P. Moin, A direct numerical simulation study on the mean velocity characteristics in turbulent pipe flow, *J. Fluid Mech.* **608**, 81 (2008).
- [23] I. Marusic, R. Mathis, and N. Hutchins, Predictive model for wall-bounded turbulent flow, *Science* **329**, 193 (2010).
- [24] F. Shan, A. Fujishiro, T. Tsuneyoshi, and Y. Tsuji, Effects of flow field on the wall mass transfer rate behind a circular orifice in a round pipe, *Int. J. Heat Mass Transf.* **73**, 542 (2014).
- [25] Z. X. Mao and J. Hanratty, The use of scalar transport probes to measure wall shear stress in a flow with imposed oscillations, *Exp. Fluids* **3**, 129 (1985).
- [26] A. Ambaric, C. Deslouis, and B. Tribollet, Frequency response of the mass transfer rate in a modulated flow at electrochemical probes, *Int. J. Heat Mass Transf.* **29**, 35 (1986).
- [27] H. Zidouh, L. Labraga, and M. W. Louis, Unsteady wall shear stress in transient flow using electrochemical method, *J. Fluid Eng.* **131**, 051403 (2009).
- [28] L. Talbot and J. J. Steinert, The frequency response of electrochemical wall shear stress probes in pulsatile flow, *Trans. ASME* **109**, 60 (1987).